Influence of chemical composition on coarsening kinetics of coherent L12 precipitates in FCC complex concentrated alloys

Thomas Rieger, Jean-Marc Joubert, Régis Poulain, Xavier Sauvage, Elie Paccou, Loïc Perrière, Ivan Guillot, Guy Dirras, Guillaume Laplanche, Mathilde Laurent-Brocq, et al.

Influence of chemical composition on coarsening kinetics of coherent $L1_2$ precipitates in FCC complex concentrated alloys

Thomas Rieger [a], Jean-Marc Joubert [a], Régis Poulain [a], Xavier Sauvage [b], Elie Paccou [b], Loïc Perrière [a], Ivan Guillot [a], Guy Dirras [c], Guillaume Laplanche [d], Mathilde Laurent-Brocq [a], Jean-Philippe Couzinié [a,*]

[a] Univ Paris Est Creteil, CNRS, ICMPE, UMR 7182, 2 rue Henri Dunant, 94320 Thiais, France

[b] Univ Rouen Normandie, INSA Rouen Normandie, CNRS, Groupe de Physique des Matériaux UMR 6634, 76000 Rouen, France

[c] Université Paris 13, Sorbonne Paris Cité, CNRS, LSPM (UPR 3407), 99 avenue JB Clément, Villetaneuse 94430, France

[d] Institut für Werkstoffe, Ruhr-Universität Bochum, D-44780 Bochum, Germany

* Corresponding author. Jean-Philippe Couzinié, jean-philippe.couzinie@cnrs.fr

Graphical abstract

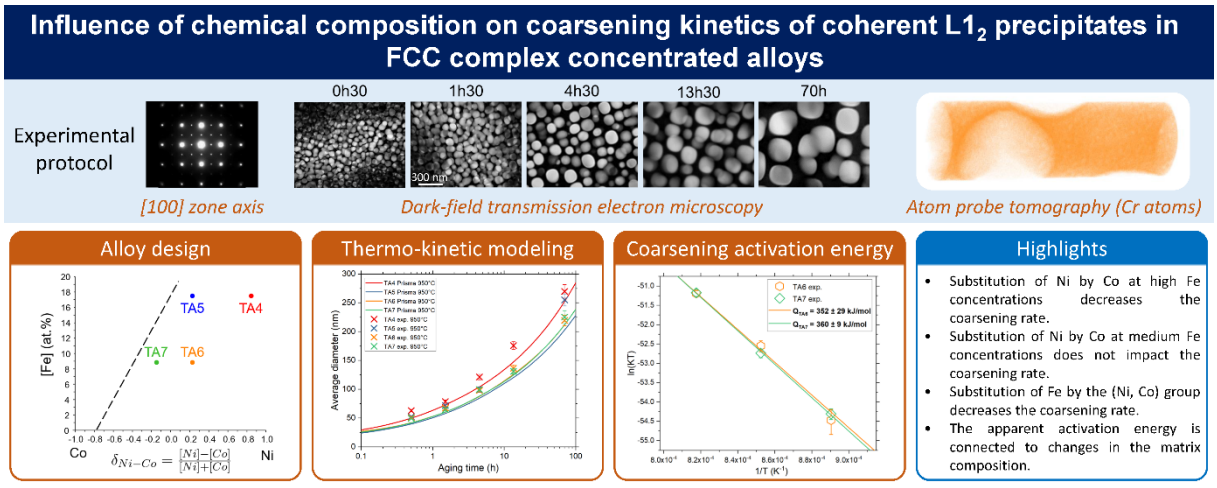

Highlights

- Substitution of Ni by Co at high Fe concentrations decreases the coarsening rate.
- Substitution of Ni by Co at medium Fe concentrations does not impact the coarsening rate.

- Substitution of Fe by the (Ni, Co) group decreases the coarsening rate.
- The apparent activation energy is connected to changes in the matrix composition.

Abstract

In this study, we report the experimental coarsening kinetics at 850, 900 and 950°C of four complex concentrated alloys in the Al–Ti–Cr–Fe–Co–Ni senary system with different chemical compositions but a similar γ' ($L1_2$) volume fraction (~35% at 950°C) in a face-centered cubic (γ, FCC) matrix. The selected alloys were specifically designed to investigate the influence of Fe additions and Ni–Co substitutions on Ostwald ripening kinetics. Atom Probe tomography (APT) was used to determine the compositions of the FCC and $L1_2$ phases, which agree very well with Calphad calculations at thermodynamic equilibrium. Thermo-kinetic modeling of $L1_2$ precipitation was carried out using the Prisma module developed by Thermo-Calc and compared with experimental results. Apparent activation energies were determined and discussed in light of diffusion-controlled coarsening models to identify the key parameters affecting Ostwald ripening. We suggest that the abnormally high apparent activation energies results from composition-dependent parameters. When the latter are accounted for, the corrected activation energies for coarsening are in better agreement with available diffusion data.

Keywords: medium-entropy superalloys; Ostwald ripening; γ/γ' microstructures; high-entropy alloys; atom probe tomography

1. Introduction

Hardening by secondary coherent precipitates is a well-known solution to strengthen metallic alloys for high-temperature applications. However, the evolution of the precipitates size and morphology with temperature and time results in a deterioration of mechanical properties during service [1]. Long-term thermal stability of the microstructure in precipitation-hardened alloys is thus a key aspect of alloy design.

Recently, precipitation of γ' ($L1_2$) phase in face-centered cubic (γ, FCC) complex concentrated alloys (CCAs) systems has gathered increasing interest [2–6]. While it

is known that the FCC+$L1_2$ microstructure is thermodynamically stable in an extended range of chemical compositions in the Al–Ti–Cr–Fe–Co–Ni system [7], its thermal stability (size and morphology) during isothermal aging is still under investigation. Zhao *et al.* first reported the coarsening rate of γ’ precipitates in a $(NiCoFeCr)_{94}Ti_2Al_4$ CCA with a low γ’ volume fraction (~13% at 800°C). Interestingly, the authors found that the coarsening rate was slower than in some Ni-based superalloys in the 750-825°C temperature range [8]. Such a low coarsening rate was attributed to a sluggish diffusion phenomena as is often claimed in the literature, owing to the chemical complexity of CCAs [9].

Since then, most of the other studies focusing on $L1_2$-strengthened CCAs showed that the coarsening kinetics of the γ’ phase is similar to that of Ni-based superalloys [8,10–12]. However, higher (apparent) activation energies have been reported [13,14] and were primarily assigned to sluggish diffusion without any consideration for other contributions that could significantly affect Ostwald ripening. Furthermore, He *et al.* have evidenced that a decrease in the γ-γ’ lattice misfit results in a decrease in the coarsening rate, pointing out an unexpected behavior [11]. Still, it is unclear whether the reduced coarsening rate is due to the change in lattice misfit or chemical composition, considering that the compositions of the γ and γ’ phases are also known to affect coarsening kinetics [15]. Therefore, the reasons for the unexpected features of Ostwald ripening in CCAs are still a matter of debate in the literature.

The Al–Ti–Cr–Fe–Co–Ni senary system is particularly interesting due to its incorporation of the binary subsystems Al–Ni and Ti–Co, which have the capability to yield FCC+$L1_2$ microstructures [16,17]. Moreover, the inclusion of Cr and Fe in these systems proves to be highly advantageous: the former can enhance corrosion resistance, while the latter contributes to cost reduction. However, the development of Ti–Co superalloys is complicated by the occurrence of detrimental phases caused by minor additions of alloying elements, including Cr and Fe. [18,19]. By analyzing the extent of the FCC+$L1_2$ phase domain in the Al–Ti–Cr–Fe–Co–Ni senary system, Rieger *et al.* [7] made two main findings. First, the quaternary Al–Ti–Co–Ni system constitutes the basis for approaching the features of higher-order systems. In this system, the FCC+$L1_2$ two-phase domain is particularly extended due to the presence of a continuous $L1_2$ phase domain, which spreads from Ni_3Al to Co_3Ti. Second, significant Cr and Fe concentrations can be reached by carefully tailoring the Ni/Co

and Al/Ti ratios. In this complex and vast system, the coarsening behavior is still widely unexplored. Few studies attempted to investigate the impact of individual elements on Ostwald ripening. For example, Adil et *al.* evidenced that Ni substitutions by Fe are correlated to an increase in the coarsening rate [10]. In contrast, substituting the (Ni, Co) base with Cr has been shown to lower the coarsening rate [20]. However, some questions remain unanswered: (1) What is the impact of Ni–Co substitutions (and, by extension Al–Ti co-substitutions) on the coarsening rate? (2) How do Fe additions – with a constant Ni/Co – ratio affect the kinetics of Ostwald ripening? (3) How do these compositional variations influence the temperature dependence of the coarsening rate? To address these questions, we investigated the coarsening behavior of the $L1_2$ phase at 850, 900, and 950°C in four alloys from the Al–Ti–Cr–Fe–Co–Ni senary system with different chemical compositions but a similar $L1_2$ volume fraction (~35% at 950°C). In order to grasp the underlying role of chemical composition and identify the key parameters affecting Ostwald ripening, the experimental results are examined under the light of two different tools. The first one is the Prisma module developed by Thermo-Calc, which is readily available and without adjustable parameters. The second one is a set of analytical models, allowing for a finer understanding of the role of each parameter.

2. Methods

2.1 Experimental

The selected alloys were specifically designed to investigate the influence of Fe additions and Ni–Co substitutions on Ostwald ripening kinetics using a Calphad-based approach [7]. The four studied alloys have the following nominal compositions in at.%:

- $Al_{7.5}Ti_5Cr_{13.1}Fe_{17.5}Co_{4.4}Ni_{52.5}$ (TA4);
- $Al_5Ti_{7.5}Cr_{13.1}Fe_{17.5}Co_{21.9}Ni_{35}$ (TA5);
- $Al_{5.5}Ti_7Cr_{13.1}Fe_{8.8}Co_{25.2}Ni_{40.4}$ (TA6);
- $Al_{4.5}Ti_8Cr_{13.1}Fe_{8.8}Co_{37.6}Ni_{28}$ (TA7).

These alloys have in common that they all contain 13.1 at.% Cr and the sum of the Ti and Al concentrations is kept constant at 12.5 at.%. Figure 1 gives a convenient way to compare the compositions of the designed alloys by considering the Fe nominal content and the Ni–Co substitutions. Two groups are identified based on their Fe

content: (TA4, TA5) with 17.5 at.% Fe and (TA6, TA7) with 8.8 at.% Fe. Within these groups, the sum of the Ni and Co concentrations remains the same (*i.e.* 56.9 at.% for (TA4,TA5) and 65.6 at.% for (TA6,TA7)) but the Ni/Co ratio changes. To ensure a similar γ' volume fraction of ~35% at 950°C in the investigated alloys, a change in Ni/Co ratio corresponds to a modification of the Ti/Al ratio [7]. The influence of Fe content on γ' coarsening kinetics was investigated by comparing the TA5 and TA6 alloys, for which Fe has been substituted by Ni and Co while maintaining the same Ni/Co ratio. Finally, the TA6 and TA7 alloys allow the exploration of compositional domains with high Co contents.

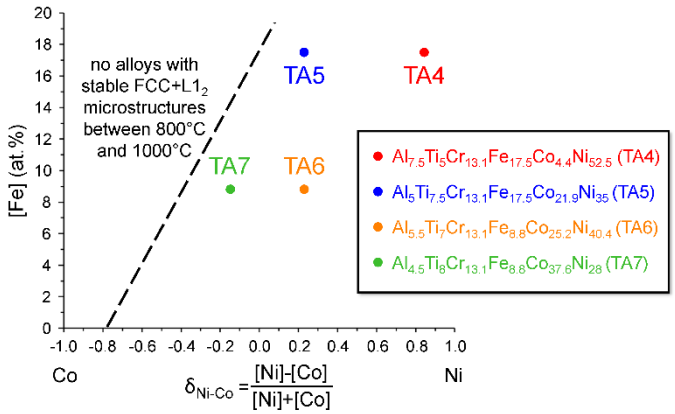

Figure 1: Nominal alloy compositions with respect to Fe content and Ni–Co substitutions ($\delta_{Ni-Co} = \frac{[Ni]-[Co]}{[Ni]+[Co]}$) for [Cr]=13.1 at.% and [Al]+[Ti]=12.5 at.%. To keep the microstructure within the FCC+L1$_2$ stability domain, Ni–Co substitutions are related to Al–Ti substitutions. The dashed line is a schematic representation of the two-phase stability limit between 800°C and 1000°C.

The alloys were processed, starting from pure metals with purity exceeding 99.5%, using induction melting under He atmosphere. The ingots were cast using gravity in a water-cooled Cu crucible. The samples were subjected to a first heat treatment above the γ'-solvus temperature in sealed silica tubes at 1150°C for 48h to ensure chemical homogeneity. The sealed tubes were then quenched and broken in water. The coarsening kinetics of the γ' phase was investigated after aging in silica tubes at 850, 900, and 950°C for times between 0.5 and 70h, followed by a water quench to retain the high-temperature microstructure. Thin foils were obtained after mechanical grinding followed by twin-jet electropolishing with a 10% $HClO_4$ – 90% methanol solution at 20V and -35°C.

Additionally, the phase stability of the TA6 and TA7 alloys was investigated using staged annealing process in a sealed silica tube filled with argon. Alloys were first introduced into a furnace at 1150°C and maintained at this temperature during 48h to ensure chemical homogeneity. They were then cooled from 1150°C to 900°C at 10°C/min and maintained at this temperature for 403h to achieve thermodynamic equilibrium before water quenching.

Microstructural characterization was performed using a JEOL 2000EX TEM in grains oriented close to the [100] zone axis. The size of each precipitate was determined as the diameter of a disc of equivalent surface area. The surface area of precipitates was determined manually using a graphics tablet and the ImageJ software. An average number of 1000 precipitates were measured for each condition. The given uncertainties correspond to two times a 99% confidence interval, which was found to include the size variations observed on multiple thin foils.

Atom Probe Tomography (APT) analyses were carried out using a CAMECA LEAP® 4000HR instrument. Specimen were prepared by focused ion beam using standard procedures. Samples were field evaporated under ultra-high vacuum (10^{-11} mbar) with electric pulses (pulse fraction of 20%, repetition rate of 200 kHz) at a temperature of 50 K. Three-dimensional (3D) reconstructions were performed using IVAS Software and data processing was performed using the Gpm3dSoft Software. The chemical compositions of both FCC and $L1_2$ phases were obtained by isotopic deconvolution of peaks in the mass spectrum.

X-ray diffraction (XRD) was carried out with a PANalytical XPert Pro diffractometer using the Co-Kα radiation at a wavelength of 0.178897 nm. Le Bail (pattern matching) refinement was finally used to determine lattice parameters using FullProf software [21]. The misfit δ was calculated from lattice parameters using the expression $\delta = 2(a_{FCC} - a_{L12})/(a_{FCC} + a_{L12})$.

2.2 Theoretical background

Coarsening in a dispersed two-phase system, also called Ostwald ripening, is a phenomenon that takes place near thermal equilibrium. Generally, coarsening results from the minimization of the sum of the interfacial and elastic strain energies [22]. However, when the lattice misfit between the matrix and the precipitates can be

neglected, the driving force for coarsening corresponds to a reduction of the total interfacial energy of the system and large particles grow at the expense of smaller ones. In the following, the presented models assume that the lattice misfit, if any, has a negligible influence on the γ' coarsening kinetics.

2.2.1 Analytical modeling of coarsening at a near-zero volume fraction

During coarsening, the temporal evolution of the average diameter of precipitates (*d*) obeys a power law as given by [23]:

$$d^n - d_0^n = Kt \tag{1}$$

where d_0 is the average diameter at the onset of coarsening, *K* is the coarsening rate, *t* is the aging time, and *n* is the power-law exponent supposed to be time-independent if no change in mechanism is considered.

In most cases, the power-law exponent *n* is close to 3 and corresponds to a coarsening process limited by bulk diffusion in the matrix [15,24–26]. The experimental coarsening rate *K* is thus usually determined using a linear fit of d^3 against aging time. It is however worth mentioning that *n* can take values closer to 2 in the case of the trans-interface diffusion-controlled coarsening mechanism [23,27,28].

The analytical expression of the coarsening rate *K* strongly relies on the used assumptions. We will hereafter describe the model of Philippe and Voorhees [24] since it considers the matrix non-ideal character and the presence of multiple elements in the alloy. Assuming that the mobility matrix is diagonal, the coarsening rate *K* can be expressed as follows [24]:

$$K = \frac{64\, V_m^{\gamma'} \sigma}{9 \sum_{i=2}^{N} G_{m,i}^{\gamma}{}'' (C_i^{\gamma'} - C_i^{\gamma})^2 / D_i} \tag{2}$$

where $V_m^{\gamma'}$ is the molar volume of the $L1_2$ phase, σ is the precipitate/matrix interfacial energy, $C_i^{\gamma'}$ and C_i^{γ} are the mole fractions of the i^{th} element in the FCC and $L1_2$ phases, respectively, *N* is the number of components in the alloy, $G_{m,i}^{\gamma}{}''$ is the

Hessian of the matrix relative to element *i*, and $D_i = D_{0,i} \exp\left(-Q_i/RT\right)$ is the diffusion coefficient of element *i* in the FCC matrix.

Assuming that the FCC solid solution is ideal and by considering *p* as the low-mobility species limiting the coarsening process, equation (2) can be simplified to [15,24]:

$$K = \frac{64\, V_m^{\gamma'} \sigma D_{0,p} C_p^{\gamma} (1 - C_p^{\gamma})}{9\, RT (C_p^{\gamma'} - C_p^{\gamma})^2} exp\left(-Q_p/RT\right) \quad (3)$$

where $D_{0,p}$ is the pre-exponential factor, and Q_p is the activation energy for diffusion in the FCC matrix. The activation energy for coarsening is usually determined with a linear fit of ln(*KT*) as a function of 1/*T*.

2.2.2 Effect of volume fraction on coarsening rate

The model developed by Philippe and Voorhees [24] is valid for precipitate volume fractions approaching zero as it considers negligible interactions between particles of the secondary phase. However, this model does not apply to alloys with a high volume fraction of precipitates as the impact of particle-particle interactions can be significant. These interactions increase the magnitude of the coarsening rate *K* if the mechanism is controlled by bulk diffusion in the matrix [26]. In this latter case, the finite volume fraction does not change the exponent of the temporal power law as observed in model alloys [29]. Therefore, the dependence of the coarsening rate *K* with volume fraction v_f can be written as:

$$K(v_f) = g(v_f) \cdot K(v_f = 0) \quad (4)$$

Where $g(v_f)$ is a monotonically increasing function of volume fraction.

In the model developed by Glicksman *et al.*, a diffusion screening length was introduced to quantify the interactions between precipitates [30]. This length is proportional to $1/\sqrt{v_f}$ for small-to-moderate values of v_f [31]. In this case, the function $g(v_f)$ can be expressed as [29]:

$$g(f_v) = \frac{27}{4}\left(\frac{2-(1-\sqrt{3f_v})\left(1-\frac{1}{\sqrt{3f_v}}+\sqrt{\frac{1}{3f_v}+\frac{1}{\sqrt{3f_v}}+1}\right)}{\left(1-\frac{1}{\sqrt{3f_v}}+\sqrt{\frac{1}{3f_v}+\frac{1}{\sqrt{3f_v}}+1}\right)^3}\right) \quad (5)$$

2.2.3 Modeling of thermodynamics and kinetics of precipitation

The thermo-kinetic modeling of precipitation was performed with the TC-Prisma module developed by Thermo-Calc [32] using the TCNI9 thermodynamic database and the MOBNI4 mobility database. The Prisma module uses the Kampmann-Wagner numerical approach [33] to deal with the simultaneous occurrence of nucleation, growth and coarsening of precipitates.

The average diameter evolution was computed with the heat treatment sequence experienced by the alloys, *i.e.*, annealing at 1150°C followed by water quenching. The cooling rate was estimated as 1350°C/min by comparison with experimental results. The obtained particle size distributions were then used as initial conditions for the coarsening heat treatments. The interfacial energy was estimated using Prisma by a first assessment of the present experimental results as well as the ones reported by Zhao *et al.* [8]. The energy was set to 10 mJ/m^2 for all alloys and for each temperature as a first approximation, which is consistent with the experimental values reported in Ni–Al alloys and Ni-based superalloys [34,35].

3. Results

3.1 Phase stability and composition

In a previous study, we already reported the thermodynamic stability of the FCC and $L1_2$ phases in the TA4 and TA5 alloys [7]. In the present work, the phase stability at 900°C of the TA6 and TA7 alloys was investigated after aging for 403h. The SEM and XRD characterizations of these alloys (Figure 2) reveal a two-phase microstructure with dark $L1_2$ precipitates embedded in a brighter FCC matrix. All the experimental data gathered on alloys after long-term annealing, including volume fractions and γ' solvus temperatures, are given in supplementary material (Table S1).

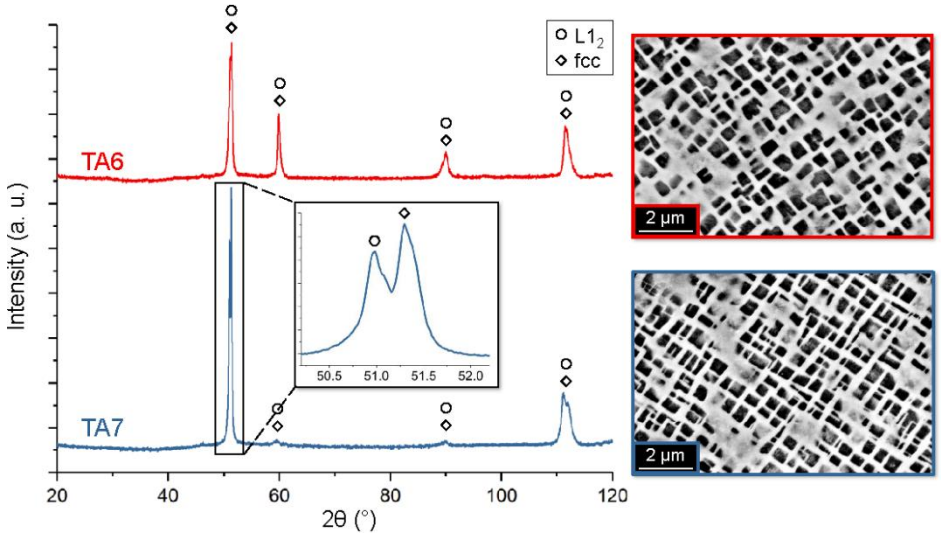

Figure 2: SEM (backscattered electrons) and XRD characterizations of the TA6 and TA7 alloys after aging at 900°C during 403h.

APT experiments were performed on the TA5 and TA6 samples and the analysis of TA5 after aging at 950°C for 1.5h is given in Fig. 3. As will be shown later, the system already reached thermal equilibrium well before 1.5h. The $L1_2$ phase is enriched in Ni, Al, and Ti, and the FCC matrix has a composition close to equimolarity for Co, Cr, Fe, and Ni with limited Al and Ti solubilities. The equilibrium compositions calculated with the TCHEA3 database are displayed with horizontal dashed lines in the concentration profile of Fig. 3 and are in good agreement with the experimental concentrations with a maximum deviation of ~2 at.%. The compositions of the FCC matrix and $L1_2$ precipitates in the TA5 and TA6 alloys aged for 1.5h at 850 and 950°C are listed in Table 1.

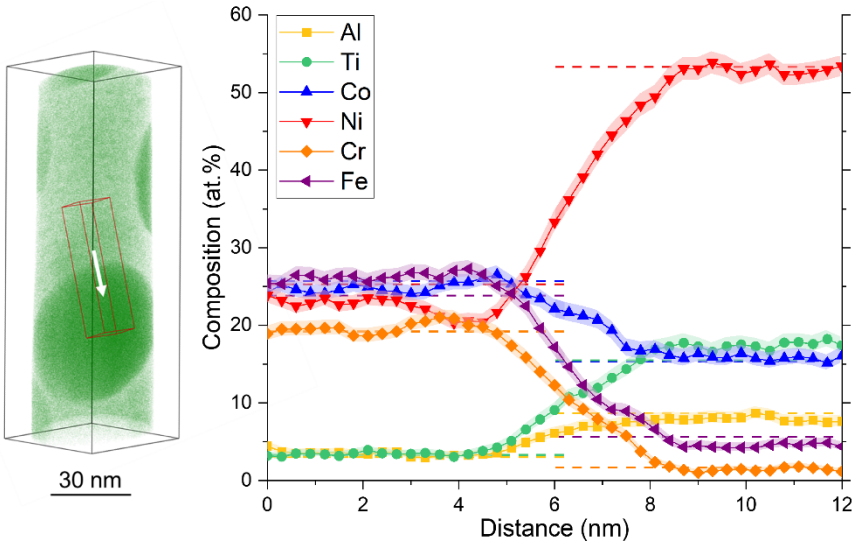

Figure 3: APT analysis of the TA5 alloy after aging at 950°C for 1.5h. (left) 3D reconstruction showing the distribution of Ti. (right) concentration profile through the FCC/$L1_2$ interface. The corresponding volume is indicated by the red parallelepiped on the reconstructed volume. The dashed lines represent the equilibrium concentrations of the FCC and $L1_2$ phases calculated with the TCHEA3 database.

Table 1: Phase compositions determined by APT for TA6 (850, 900 and 950°C) and TA5 (950°C) after aging during 1.5h. The given compositions (at.%) were determined by extraction of sub-volumes inside the matrix and precipitates. The experimental uncertainties are smaller than 0.2 at.%.

at.% (± 0.2)		Al	Ti	Cr	Fe	Co	Ni
TA6	FCC	2.8	1.5	21.4	15.0	33.0	26.1
(850°C)	$L1_2$	10.2	15.1	1.6	2.0	14.8	56.3
TA6	FCC	3.5	2.0	19.7	14.3	31.9	28.6
(900°C)	$L1_2$	9.8	15.5	1.7	2.2	15.0	55.7
TA6	FCC	3.8	2.4	21.0	13.6	29.9	29.2
(950°C)	$L1_2$	9.5	15.2	2.0	2.4	15.8	55.5
TA5	FCC	4.1	3.4	19.1	23.8	23.9	25.6
(950°C)	$L1_2$	7.7	16.8	1.6	4.9	16.2	52.6

3.2 Microstructure evolution during isothermal aging

The coarsening behavior of the $L1_2$ phase in the TA6 and TA7 alloys has been investigated after isothermal annealing for times ranging from 0.5h to 70h at 850, 900, and 950°C, while that of the TA4 and TA5 alloys were studied at 950°C.

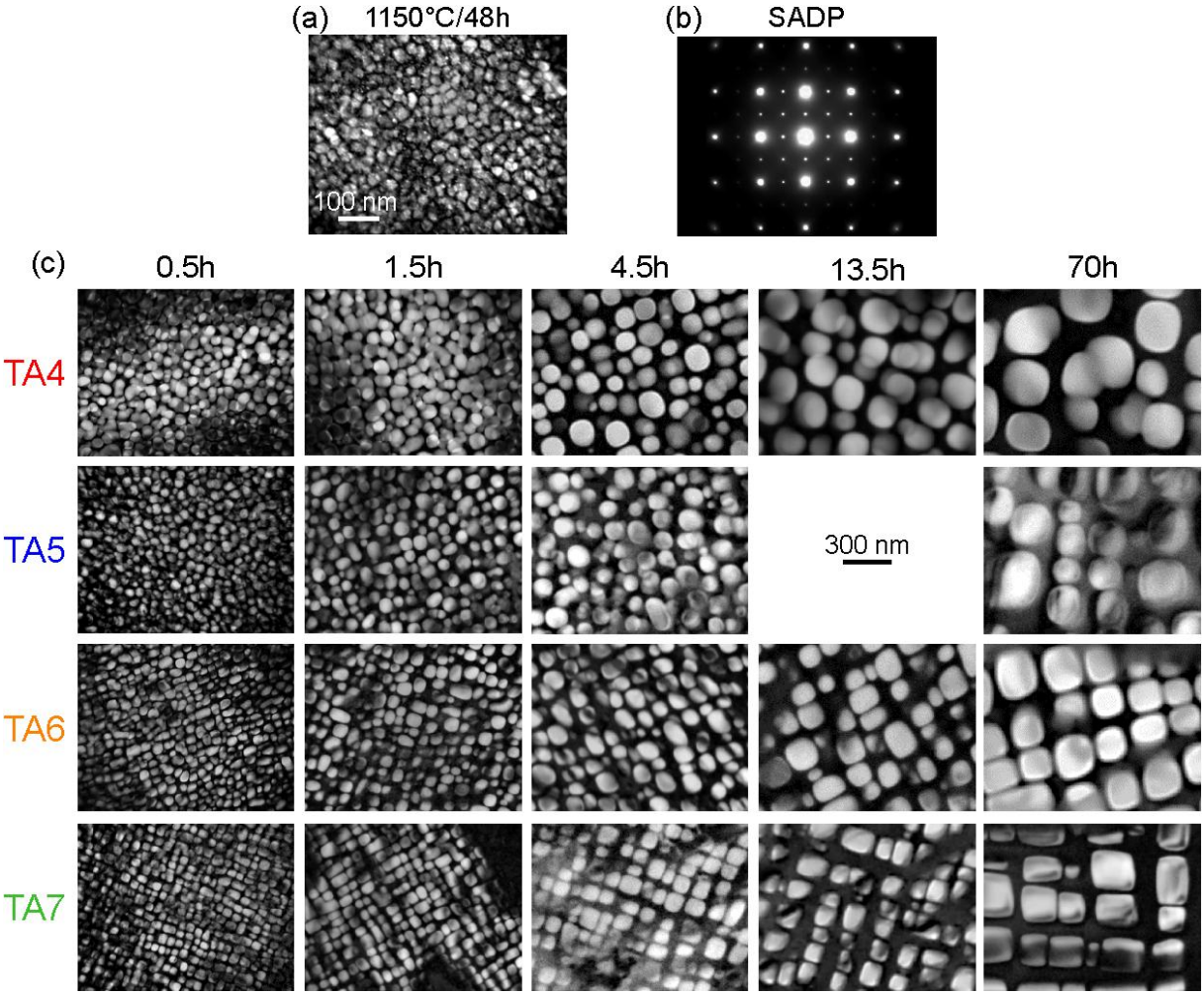

Figure 4: Coarsening of $L1_2$ precipitates at 950°C. All the samples were tilted close to the [100] zone axis before imaging. (a) Dark-field TEM micrograph of TA6 after solution annealing at 1150°C for 48h and water quenching. (b) SADP of the TA6 alloy with the presence of $L1_2$ superlattice reflections. (c) Dark-field TEM micrographs of the alloys aged at 950°C. The scale is the same for all micrographs.

After solution annealing (1150°C for 48h) and water quenching, a large volume fraction of fine precipitates is observed in all alloys (Fig. 4a). This latter dark field TEM micrograph, where the precipitates are bright and the matrix darker, was recorded by selecting a superlattice reflection of the $L1_2$ precipitates in the selected area diffraction pattern (SADP) shown in Fig. 4b. Except for some carbides and/or sulfides (not shown here), resulting from the presence of impurities in the raw metals, only FCC and $L1_2$ phases were observed. The microstructural evolution of the four alloys upon aging at 950°C is shown in Fig. 4c. Additional TEM images for TA6 and TA7 that were aged at 850°C and 900°C can be found in Fig. S1 of the supplementary material. The distribution of precipitates is homogeneous within the FCC matrix and the average size of the ordered phase increases drastically with

aging time (Fig. 4c). The mean diameter of the $L1_2$ precipitates, obtained by TEM, after each heat treatment is provided in Table 2. After 70h, the initially spherical precipitates of the TA4 and TA5 alloys become slightly cuboidal. In contrast, this transition is observed after only 1.5h in TA6 and TA7. The cuboidal morphology of the precipitates is more pronounced in TA7 followed by TA6, TA5 and TA4, indicating that TA4 and TA7 exhibit the smallest and largest lattice misfits, respectively.

Table 2: Experimental mean precipitate diameters measured by TEM after isothermal annealings at different temperatures for times comprised between 0.5h and 70h. The size of each precipitate was determined as the diameter of a disc of equivalent surface area. The given uncertainties correspond to two times a 99% confidence interval.

Annealing		**Mean diameter (*d*) of precipitates (nm)**			
***T* (°C)**	***t* (h)**	**TA4**	**TA5**	**TA6**	**TA7**
reference state prior aging		-	-	25 ± 1	19 ± 2
850	0.5	-	-	31 ± 1	24 ± 1
	1.5	-	-	40 ± 2	28 ± 1
	4.5	-	-	52 ± 2	41 ± 2
	13.5	-	-	56 ± 2	50 ± 2
	70	-	-	76 ± 3	81 ± 3
900	0.5	-	-	38 ± 2	35 ± 1
	1.5	-	-	53 ± 2	48 ± 2
	4.5	-	-	64 ± 2	60 ± 2
	13.5	-	-	83 ± 3	83 ± 4
	70	-	-	148 ± 5	134 ± 5
950	0.5	63 ± 2	52 ± 2	51 ± 2	49 ± 2
	1.5	78 ± 3	72 ± 3	67 ± 3	65 ± 2
	4.5	121 ± 5	99 ± 4	98 ± 4	100 ± 3
	13.5	176 ± 7	-	136 ± 6	131 ± 4
	70	270 ± 12	255 ± 10	219 ± 9	225 ± 11

The experimental particle size distributions (PSDs) obtained from TEM investigations are shown as bar charts in Fig. 5 and compared to those calculated within the scope of the LSW (Lifshitz-Slyozov-Wagner) model (dashed lines) and simulated with TC-Prisma (solid lines). The former is based on a mean-field approach considering a dilute alloy without interaction between particles (*i.e.,* the volume fraction of precipitates approaches zero [25]) while the latter rely on the Kampmann-Wagner

Numerical approach as described in Section 2.2.3. The simulated results take into account the interactions between particles through the volume fraction. The PSDs simulated with TC-Prisma are more symmetric than the LSW ones, which is expected considering the interactions between particles resulting from a finite volume fraction of precipitates [36]. Generally, the experimental PSDs are similar to the TC-Prisma simulations (Fig. 5) and the apparent self-similarity of all experimental distributions for different aging times suggests that coarsening is the main process controlling the size distribution of the precipitates.

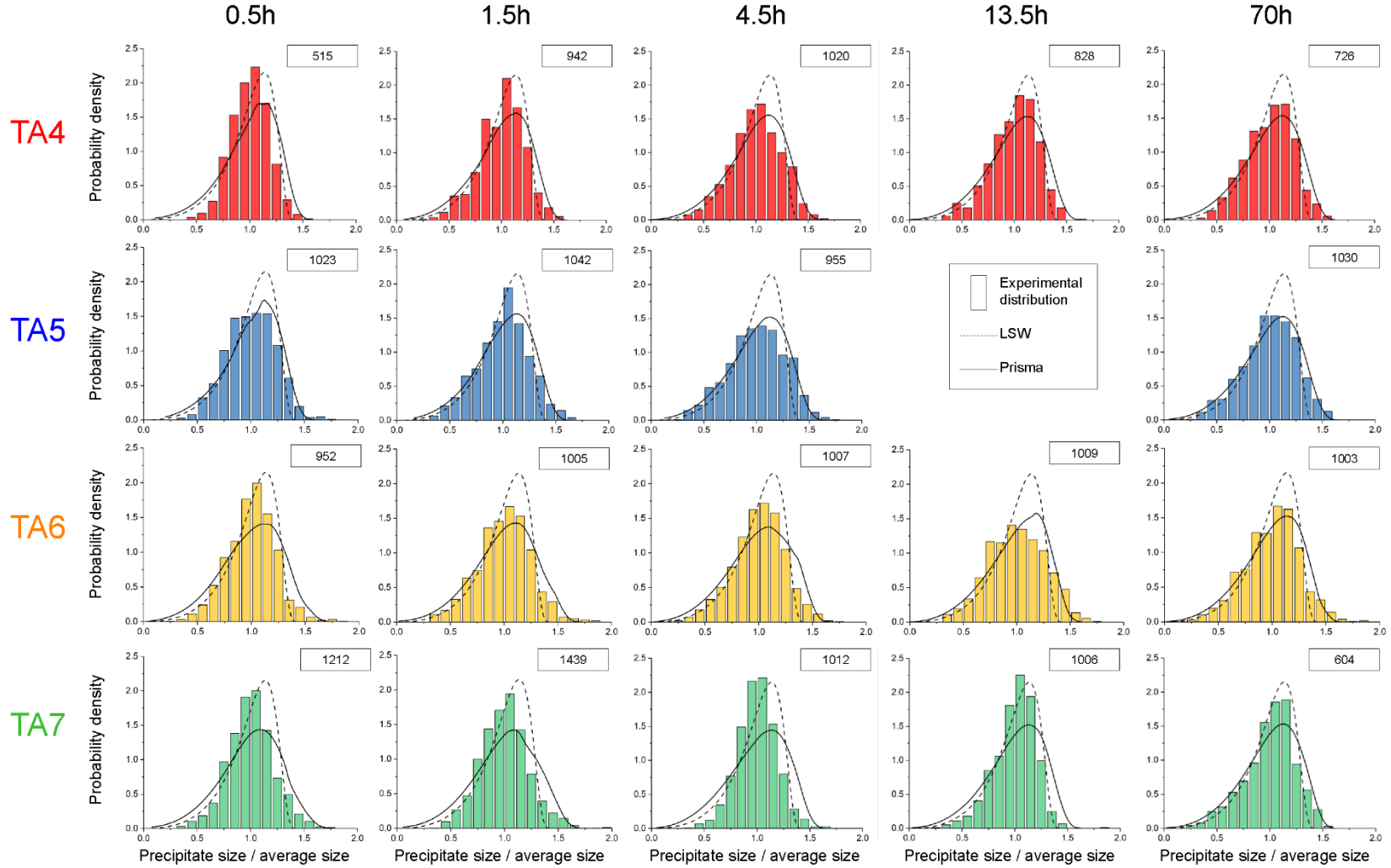

Figure 5: Temporal evolutions of particle size distributions (PSDs) of the $Al_{7.5}Ti_5Cr_{13.1}Fe_{17.5}Co_{4.4}Ni_{52.5}$ (TA4), $Al_5Ti_{7.5}Cr_{13.1}Fe_{17.5}Co_{21.9}Ni_{35}$ (TA5), $Al_{5.5}Ti_7Cr_{13.1}Fe_{8.8}Co_{25.2}Ni_{40.4}$ (TA6) and $Al_{4.5}Ti_8Cr_{13.1}Fe_{8.8}Co_{37.6}Ni_{28}$ (TA7) alloys at 950°C. Here, the precipitate sizes are normalized by the mean size (Table 2) to ease the comparison between different alloys and aging times. The number of analyzed precipitates is framed as an inset in each PSD. The experimental bar charts are systematically compared to PSDs that were computed using the LSW theory (dashed lines) or simulated by thermo-kinetic modeling using the Thermo-Calc Prisma module (solid lines).

3.3 Precipitation simulations using TC-Prisma

After solution annealing, the evolution of the $L1_2$ volume fraction during cooling at different rates was assessed with TC-Prisma (Fig. 6a). After water quenching from 1150°C, corresponding to cooling within 50s, the TC-Prisma simulations suggest that ~47% volume fraction of $L1_2$ phase has precipitated in the FCC matrix (green curve in Fig. 7a). This finding is corroborated by our experimental observations, with the presence of a large $L1_2$ volume fraction after quenching (Fig. 4a).

From these simulations, we established the isothermal TTT diagram displayed in Fig. 6b. The latter indicates that 99% of the equilibrium $L1_2$ volume fraction is formed within ~100s for temperatures ranging from 850°C to 950°C (Fig. 6b for the TA4 alloy). Therefore, the equilibrium $L1_2$ volume fraction is reached very quickly during isothermal aging and the increase in size observed experimentally during aging is mainly related to coarsening (during which the $L1_2$ volume fraction remains nearly constant).

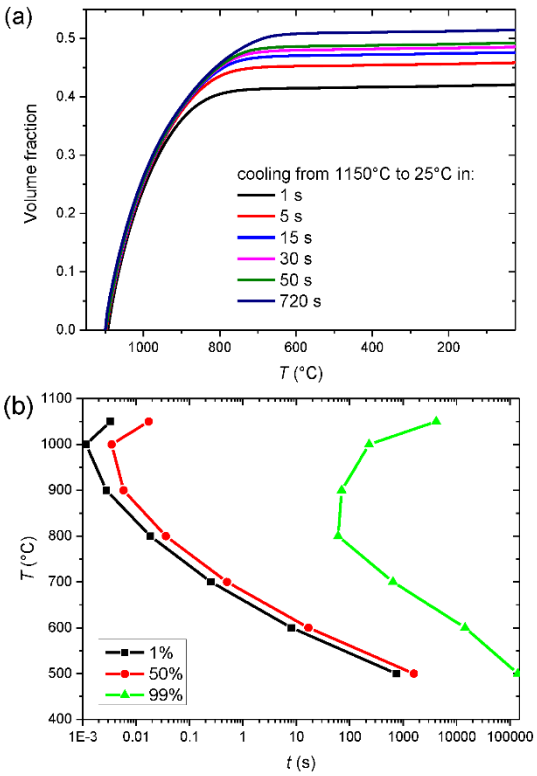

Figure 6: Simulation of $L1_2$ precipitation in the TA4 alloy. (a) Evolution of the $L1_2$ volume fraction during cooling from 1150°C to room temperature in 1s, 5s, 15s, 30s, 50s and 720s. The experimental quenching rate was estimated as 1350°C/min, corresponding to a cooling time of 50s (green curve).

(b) Calculated isothermal TTT diagram showing the start (1%), mean (50%), and end (99%) of $L1_2$ precipitation.

Using the results of the 50s simulation as inputs, we subsequently simulated the evolutions of $L1_2$ volume fraction upon isothermal aging at different temperatures. The evolutions of the experimental and simulated average diameters with annealing time are shown in Fig. 7. Overall, the experimental data are well reproduced by TC-Prisma simulations except for TA6 at 850°C and TA5 at 950°C for intermediate aging times. TA6 and TA7 exhibit a very similar coarsening behavior at the three investigated temperatures. At 950°C (Fig. 7b), TA4 is predicted to have larger precipitates than the other alloys, which is also supported by the experimental results.

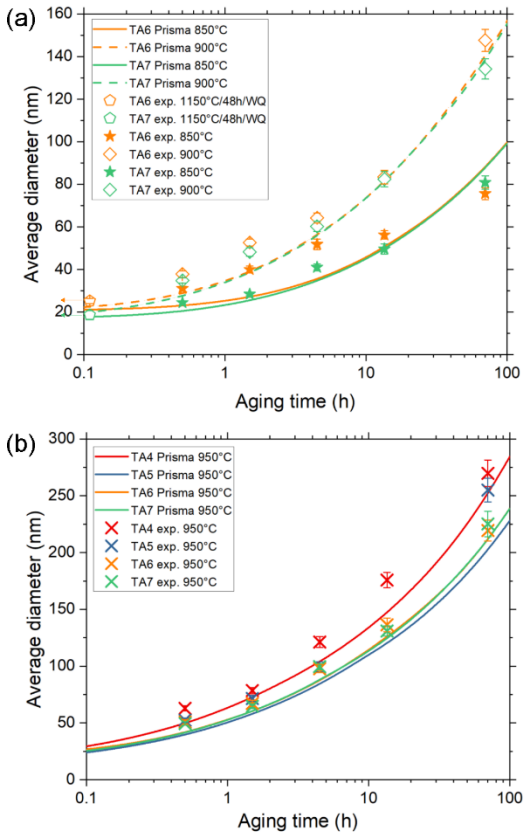

Figure 7: Comparison of the temporal evolutions of the average precipitate diameter predicted by TC-Prisma (lines) and experimental values (symbols). (a) TA6 and TA7 at 850°C and 900°C. (b) TA4, TA5, TA6 and TA7 at 950°C.

3.4 Coarsening kinetics at different temperatures

As coarsening is the primary operating mechanism during aging, the power-law exponent can be determined by fitting equation (1) to the experimental values shown in Fig. 8. The obtained *n*-values are reported in Fig. 8 for each alloy and annealing temperature.

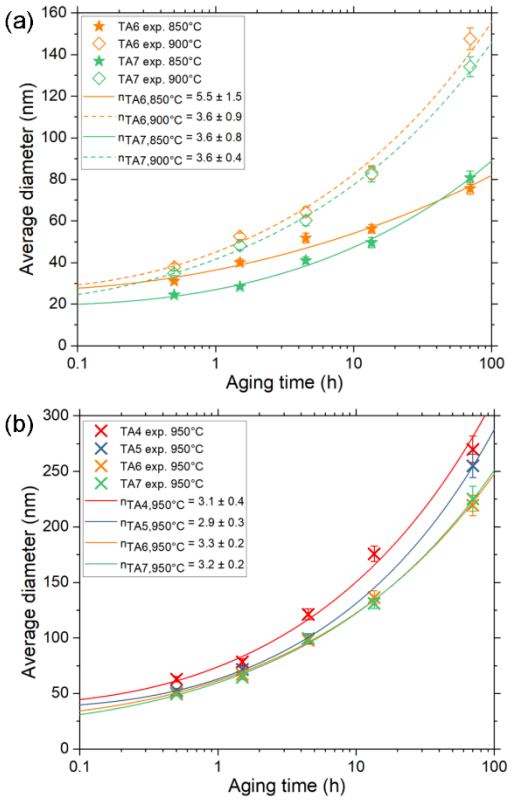

Figure 8: Power-law fits (lines) of experimental data (symbols) with respect to equation 1. (a) TA6 and TA7 at 850°C and 900°C. (b) TA4, TA5, TA6 and TA7 at 950°C. The refined n-values are provided in the legend.

Given experimental and fitting uncertainties, *n* is close to 3 at the exception of TA6 at 850°C, regardless of alloy composition and aging temperature. Therefore, the trans-interface diffusion-controlled coarsening mechanism can already be ruled out since none of the power-law exponents are close to 2. Overall, we can reasonably assume that $n = 3$, corresponding to a coarsening process limited by bulk diffusion in the FCC matrix. Double logarithmic plots of d^3 *versus* aging time in Fig. 9 thus yield straight lines (generally for $t > 1$h when $d^3 >> d_0^3$) with a slope of one and ordinates at $t = 1$h related to the coarsening rates (K in equation (1)), *e.g.* at $t = 1$h, $d^3 = 3.2 \times 10^5$ nm^3, corresponding to $K = 8.9 \times 10^{-26}$ m^3/s. In terms of coarsening resistance, TA6 and

TA7 behave similarly at all temperatures and perform better than TA4 and TA5 at 950°C.

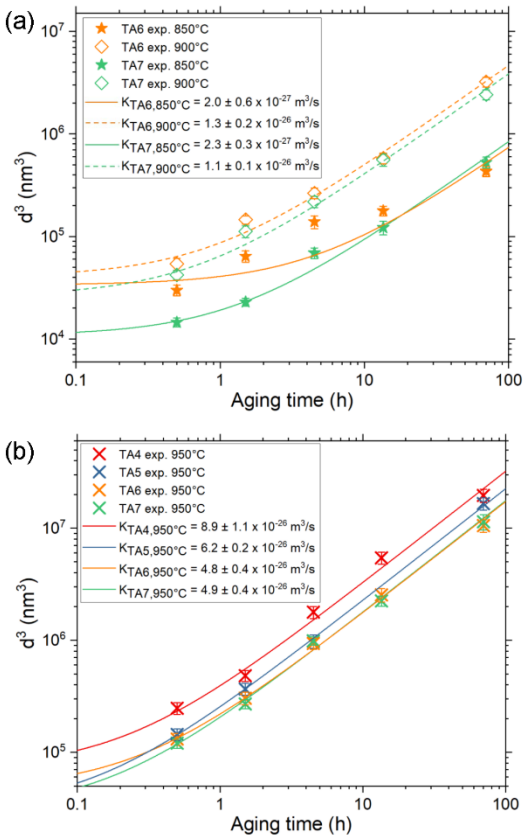

Figure 9: Power-law fits (lines) of experimental data (symbols) with respect to equation 1 and using n = 3. (a) TA6 and TA7 at 850°C and 900°C. (b) TA4, TA5, TA6 and TA7 at 950°C.

The analysis of three temperatures for TA6 and TA7 allows the determination of the apparent activation energy for coarsening. By fitting a straight line through the ln(KT)-*versus*-1/T data in Fig. 10, the apparent activation energies are similar for both alloys with Q_{TA6} = 352 ± 29 kJ/mol and Q_{TA7} = 360 ± 9 kJ/mol.

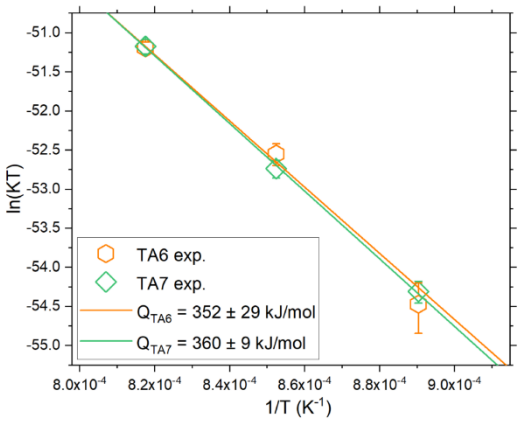

Figure 10: Arrhenius plot and determination of the activation energy for $L1_2$ coarsening in TA6 and TA7.

4. Discussion

4.1 Comparison between experimental and calculated results

4.1.1 Chemical composition

Chemical compositions of both FCC and $L1_2$ phases in TA5 (950°C / 1.5h) and TA6 (850, 900, 950°C / 1.5h) have been determined experimentally with APT. The obtained results are compared with equilibrium compositions calculated using the TCHEA3 database in Fig. 11.

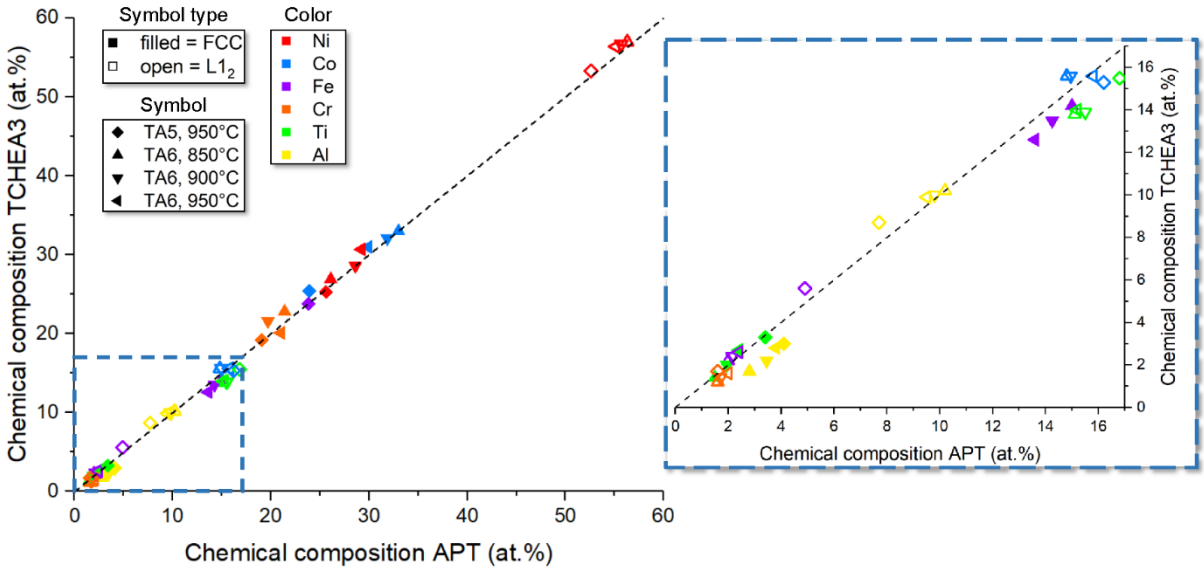

Figure 11: Comparison of the chemical compositions obtained with APT and equilibrium values computed with the TCHEA3 database for TA5 and TA6 at annealed at various temperatures. Open

and filled symbols refer to $L1_2$ and FCC concentrations, respectively. The dashed line with a slope of one and going through the origin represents the equality of computed and experimental values.

Computed and experimental compositions are in good agreement and the maximum deviation is not greater than 2 at.%. Equilibrium chemical compositions computed with the TCHEA3 database thus represent a very good approximation of experimental compositions during coarsening.

4.1.2 Volume fractions

Volume fractions are difficult to measure accurately using TEM in alloys with moderate to high volume fractions. However, assuming that both phases have similar molar volumes, the chemical compositions measured by APT can provide an approximate volume fraction of precipitates using a lever rule (Table 3).

Table 3: Volume fraction of $L1_2$ precipitates for the samples annealed for 1.5h, calculated for each element using experimental compositions of the phases determined by APT. Also shown are the average $L1_2$ volume fractions as well as those computed using Thermo-Calc.

							$L1_2$ volume fractions	
	Al	**Ti**	**Cr**	**Fe**	**Co**	**Ni**	**Average**	**TCHEA3**
TA6 (850°C)	36%	40%	42%	48%	37%	47%	43%	45%
TA6 (900°C)	32%	37%	37%	45%	33%	44%	40%	42%
TA6 (950°C)	30%	36%	42%	43%	26%	43%	38%	38%
TA5 (950°C)	25%	31%	34%	33%	26%	35%	32%	35%

Table 3 shows that the volume fractions calculated with the TCHEA3 database are in good agreement with the experimental values determined by APT.

4.1.3 Potential effect of composition on interfacial energy

As shown previously, TC-Prisma simulations, which neglect any effect of lattice misfit on the $L1_2$ coarsening kinetics, can reasonably describe the PSD evolution with time and temperature (Fig. 5). The shape of the PSDs shows that Ostwald ripening is occurring with a negligible amount of coalescence between precipitates, which is known to widen the PSDs and introduce a positive skewness [37,38]. The deviations observed between the simulations and experimental results can be explained, at least partially, by the chosen value of the interfacial energy σ, which was taken as 10 mJ/m^2 for all simulations. It is well known that σ changes with temperature and composition [35,39,40], thus affecting the coarsening rate K (eq. 2). The interfacial energy is usually calculated from experimental coarsening data, assuming ideal

behavior of the solid solution. However, calculating the interfacial energy that way can lead to overestimated values, as pointed out by Calderon *et al.* [15].

The interfacial energy is a key input parameter of all thermo-kinetic calculations. In other words, one needs predictive tools to estimate the interfacial energy. The analysis by nearest neighbors and the broken bond model are often used to calculate its magnitude [35] but can lead to contradictory results [34].

In their study, Fahrmann and Metzler used TC-Prisma with different interfacial energy values to match their experimental results [41]. In our case, the coarsening rates (K_{model}) were simulated assuming $\sigma = 10$ mJ/m^2. Considering that K is directly proportional to σ (equation 2), the latter could be corrected to better fit our experimental results (K_{exp} in Table 4).

Table 4: Experimental and computed (σ = 10 mJj/m^2) coarsening rates at 950°C. The corrected interfacial energies are calculated from the comparison with experimental results, according to equation 2.

Alloy	K_{model} (× 10^{-27} m^3/s)	K_{exp} (× 10^{-27} m^3/s)	Ratio	Corrected σ (mJ/m^2)
TA4	63.8	89.0	1.39	13.9
TA5	33.2	62.4	1.88	18.8
TA6	37.9	47.7	1.26	12.6
TA7	37.9	48.7	1.28	12.8

Within this approximation and by considering the experimental errors, the alloys have interfacial energies comprised between 10 and 20 mJ/m^2 (Table 4). These values are in the lower end of standard Ni-based superalloys [35].

Liu *et al.* showed, using first-principles calculations, that the substitution of Al by Ti in Ni_3Al is correlated with a higher interfacial energy [39], which is consistent with experimental literature data on superalloys [35,42]. The higher Ti/Al ratio in the $L1_2$ phase of TA5 compared to TA6 (Table 1) might thus be responsible for the higher interfacial energy of the former, resulting in a higher coarsening rate. However, it is not clear whether this result can be extended to more complex alloys, such as that of the present study. Systematic studies like the one conducted by Liu *et al.* [39] are thus needed in the complex compositional space of multicomponent alloys in order to provide a definitive answer.

4.2 Influence of misfit on coarsening

All models presented in section 2.2 assume that the driving force for coarsening corresponds to the minimization of interfacial energy. However, in stressed systems, the minimization of elastic energy due to a difference in lattice parameters between matrix and precipitates can act as an additional driving force, thus altering the amplitude of the power law [43–45]. The effect of lattice misfit on coarsening kinetics of $L1_2$ precipitates in a FCC matrix is complex. When the lattice mismatch is small, the elastic stresses should not alter the value of the coarsening rate constant [15]. Li *et al.* identified a misfit threshold of ~0.4% in Ni-based superalloys, above which the lattice misfit starts to significantly affect the coarsening behavior [35]. The origin of such behavior could be related to the effect of coherency strains on interfacial energy, which would influence the driving force for coarsening. In $L1_2$-strengthened CCAs, He *et al.* have evidenced that an increase in lattice misfit results in an increase of the coarsening kinetics [11]. A similar trend was already observed by Conley et *al.* in the Ni–Al–Mo system [46]. However, there is no definitive proof that the difference in coarsening rate is caused by the change in lattice misfit since the slight change in chemical composition to obtain it can have a significant impact on the interfacial energy (section 4.1.3).

The morphological characteristics of misfitting precipitates are governed by the interplay between interfacial energy and the minimization of strain energies arising from lattice mismatch between the precipitate and the matrix. In the absence of elastic stress, the equilibrium shape of a particle is primarily determined by the interfacial energy, resulting in a spherical morphology. However, with the progression of precipitate coarsening, the relative influence of elastic energy on the overall energy increases, impacting the equilibrium shape [47]. Due to the elastic anisotropy of FCC solid solutions, the particles will develop regions of high curvature along the elastically hard <110> directions and regions of low curvature along the <100> directions. Consequently, one anticipates a gradual transition from a spherical morphology to a cubic one as the particle size increases, with a transition occurring for lower sizes in the case of higher misfits. From the TEM analyses of the precipitates in Fig. 4, TA6 and TA7 are expected to have higher misfits than TA4 and TA5 since the $L1_2$ precipitates exhibit a more pronounced cubic morphology.

Experimental values determined by XRD at room temperature confirm this tendency after 403-h anneals at 900°C (Table 5), *i.e.*, the coherency across the FCC/$L1_2$ interfaces results in compressive and tensile stresses in the $L1_2$ and FCC phases, respectively, the magnitude of which increases in the order TA4 < TA5 < TA6 < TA7. Recently, Llewelyn *et al.* showed that, the misfit is expected to decrease with increasing temperatures in (Ni, Co)-based superalloys, which share many common features with the present alloys [48]. The misfit during coarsening is thus expected to be lower than that measured at room temperature.

As the hydrostatic compressive stresses within the $L1_2$ precipitates increases with increasing the interfacial energy through the Gibbs-Thomson effect and that the lattice misfit introduces additional compressive stresses at the interface, one may anticipate that the latter contributes to accelerate the coarsening kinetics (as was evidenced by He et al. [11]). Since our results show the opposite trend (the coarsening kinetics in our TA alloys decreases with increasing lattice misfit), we consider that the lattice misfit does not significantly contribute to the coarsening kinetics and that other factors govern the coarsening kinetics, as will be addressed in section 4.5.

Table 5: Experimental lattice parameters and misfits of the alloys determined with XRD at room temperature after heat treatment at 900°C during 403h. The uncertainty on the given misfit values is estimated to be lower than 30%.

	a_{FCC} (nm)	a_{L12} (nm)	misfit (%)
TA4	0.3588	0.3602	0.37%
TA5	0.3589	0.3606	0.54%
TA6	0.3578	0.3600	0.61%
TA7	0.3577	0.3600	0.64%

Table 6: Activation energy for coarsening (Q), coarsening rate (determined with precipitate diameters) K_d, aging temperature T, volume fraction V_f and volume-fraction-corrected coarsening rates (K_d (V_f = 0)) using the model of Glicksmann et al. *[30]. The volume fractions given for the alloys of this study were calculated using the TCHEA3 database.*

Alloy	Q (kJ/mol)	K_d (m^3/s)	T (°C)	V_f (%)	K_d ($V_f = 0$)	Ref.
$Al_{7.5}Ti_5Cr_{13.1}Fe_{17.5}Co_{4.4}Ni_{52.5}$ (TA4)		8.9×10^{-26}	950	30	3.5×10^{-26}	This work
$Al_5Ti_{7.5}Cr_{13.1}Fe_{17.5}Co_{21.9}Ni_{35}$ (TA5)		6.2×10^{-26}	950	35	2.4×10^{-26}	This work
$Al_{5.5}Ti_7Cr_{13.1}Fe_{8.8}Co_{25.2}Ni_{40.4}$ (TA6)	352	2.0×10^{-27}	850	45	7.0×10^{-28}	This work
		1.3×10^{-26}	900	42	4.6×10^{-27}	
		4.8×10^{-26}	950	38	1.8×10^{-26}	
$Al_{4.5}Ti_8Cr_{13.1}Fe_{8.8}Co_{37.6}Ni_{28}$ (TA7)	360	2.3×10^{-27}	850	43	8.2×10^{-28}	This work
		1.1×10^{-26}	900	39	4.0×10^{-27}	
		4.9×10^{-26}	950	34	1.9×10^{-26}	
$Al_{13.6}Ni_{86.4}$	278	1.0×10^{-29}	600	-	-	[49]
		1.1×10^{-27}	725	-	-	
		4.6×10^{-27}	775	-	-	
		9.3×10^{-27}	800	-	-	
		2.3×10^{-26}	825	-	-	
$Al_{9.7}Cr_{17.6}Ni_{72.7}$	336	4.9×10^{-28}	750	40	1.8×10^{-28}	[50]
		3.4×10^{-27}	800	35	1.3×10^{-27}	
		1.5×10^{-26}	850	23	6.5×10^{-27}	
$Al_{10}Co_{80}W_{10}$	295	5.6×10^{-28}	800	-	-	[51]
		1.1×10^{-26}	900	-	-	
Inconel 939	266	2.7×10^{-28}	750	-	-	[52]
		1.7×10^{-27}	810	-	-	
		4.2×10^{-27}	870	-	-	
		2.4×10^{-26}	930	-	-	
CMSX-4	272	3.1×10^{-27}	850	-	-	[53]
		9.9×10^{-27}	900	-	-	
		2.0×10^{-26}	925	-	-	
		3.2×10^{-26}	950	-	-	
$Al_8Ti_{2.6}Cr_{13.6}Co_{20.1}Ni_{51}Mo_{3.2}Ta_{1.3}$		1.2×10^{-26}	900	38	4.4×10^{-27}	[34]
$Al_{6.7}Ti_{2.5}Cr_{17.8}Co_{20.1}Ni_{48.4}Mo_{3.1}Ta_{1.3}$		9.9×10^{-27}	900	35	3.8×10^{-27}	
$Al_4Ti_2Cr_{23.5}Fe_{23.5}Co_{23.5}Ni_{23.5}$	276	4.8×10^{-29}	750	25.5	2.0×10^{-29}	[8]
		8.7×10^{-29}	775	17.5	4.1×10^{-29}	
		1.8×10^{-28}	800	12.7	9.1×10^{-29}	
		4.1×10^{-28}	825	10.1	2.2×10^{-28}	
$Al_{0.1}Ti_{0.2}CrFeCoNi_2$		2.0×10^{-28}	800	18.6	9.2×10^{-29}	[11]
$Al_{0.15}Ti_{0.15}CrFeCoNi_2$		1.5×10^{-28}	800	15.1	7.3×10^{-29}	
$Al_{0.2}Ti_{0.1}CrFeCoNi_2$		1.5×10^{-28}	800	12.9	7.6×10^{-29}	
$Al_{9.9}Ti_{3.5}Cr_{5.9}Co_{37.6}Ni_{35.4}Mo_{4.9}Ta_{2.8}$	360	1.7×10^{-26}	900	-	-	[13]
		1.1×10^{-25}	950	-	-	
		3.1×10^{-25}	1000	-	-	
$Al_{7.8}Ti_{7.2}Cr_{12.2}Fe_0Co_{20.6}Ni_{52.2}$		2.3×10^{-26}	900	65	-	[10]
$Al_{7.8}Ti_{7.2}Cr_{12.2}Fe_5Co_{20.6}Ni_{47.2}$		2.7×10^{-26}	900	60	-	
$Al_{7.8}Ti_{7.2}Cr_{12.2}Fe_{11.5}Co_{20.6}Ni_{40.7}$		3.6×10^{-26}	900	60	-	

$B_{0.1}Al_6Ti_6Cr_{15}Fe_{13}Co_{30}Ni_{29.9}$	378	2.8×10^{-28}	800	-	-	[14]
		1.1×10^{-26}	900	-	-	
		1.8×10^{-25}	1000	-	-	

4.3 Comparison with alloys reported in the literature

To compare the results found in the literature with those of the current study, the coarsening rates from the literature were corrected using the following relationships: $K_d = 8\,K_r$ and $K_d = {}^{8}/_{\sqrt[3]{\pi}}K_a$, where K_d, K_r, and K_a are the coarsening rates measured with the diameter, radius of rounded precipitates, and edge length of cubic precipitates, respectively. It is however worth noting that the apparent activation energy for coarsening does not depend on the measurement method. Coarsening data for binary and ternary alloys, superalloys, and CCAs are summarized in Table 6.

To allow a fair comparison between the results reported in the literature, the equivalent coarsening rate at zero-volume fraction (K_d (V_f = 0)) is calculated using equation (5) in Table 6. Here, binary and ternary alloys are found to have higher coarsening rates than complex concentrated alloys. For instance, at 850°C, TA6 and TA7 exhibit K_d (V_f = 0)-values almost an order of magnitude lower than those of the ternary $Al_{9.7}Cr_{17.6}Ni_{72.7}$ alloy. However, it should be noted that the coarsening rates of CCAs are comparable to those of Ni-based and (Ni,Co)-based superalloys, even in the absence of refractory elements, which can considerably improve the coarsening resistance [54].

The study conducted by Meher *et al.* [34] is of particular interest, since the chemical compositions of their alloys ($Al_8Ti_{2.6}Cr_{13.6}Co_{20.1}Ni_{51}Mo_{3.2}Ta_{1.3}$ and $Al_{6.7}Ti_{2.5}Cr_{17.8}Co_{20.1}Ni_{48.4}Mo_{3.1}Ta_{1.3}$ in Table 6) are comparable to that of TA6 ($Al_{5.5}Ti_7Cr_{13.1}Fe_{8.8}Co_{25.2}Ni_{40.4}$). Surprisingly these three alloys exhibit similar coarsening rates at 900°C despite the absence of refractory elements in the present studies. This result illustrates that the control of CCAs' composition may help to reduce the cost and density of alloys without any loss in coarsening resistance.

4.4 Effect of Fe content and Ni/Co ratio on coarsening kinetics in CCAs

In the present study, the effect of Fe content on coarsening kinetics can be assessed by comparing the *K*-values of TA5 and TA6, the Ni/Co ratio being similar in the two grades. Here, our results clearly provide evidence that an increase in Fe content is correlated with an increase in the coarsening rate at 950°C, in line with results reported in the literature [10,55]. On the other hand, the impact of Ni –Co substitutions – which are here accompanied by Al–Ti substitutions to keep the alloy microstructure within the stable FCC+$L1_2$ domain [7] – is noticeable at higher Fe content. Therefore, a significant decrease in the coarsening rate is found between TA4 and TA5 at 950°C, with [Fe] = 17.5 at.%, and for which Ni is highly substituted to Co. The same tendency is, however, not observed in TA6 and TA7 with [Fe] = 8.8 at. %, the coarsening rates of these two alloys being similar.

4.5 Correction of the apparent activation energies for the $L1_2$ coarsening kinetics

The activation energies (*Q*) for diffusion of elements in similar FCC-structured systems are given in Table 7. The apparent *Q*-value for coarsening in TA6 and TA7 (~360 kJ/mol) is 12-57% higher than those of bulk diffusion (~230-320 kJ/mol). Other authors have also reported surprisingly high apparent activation energies for coarsening in CCAs (Table 6).

Table 7: Activation energies for bulk diffusion of different species in Ni and various CCAs.

Species	Alloy	Measure	Q (kJ/mol)	Ref.
Cr	$(NiCoFeCr)_{92}Al_8$	tracer	283	[56]
Fe	$(NiCoFeCr)_{92}Al_8$	tracer	280	
Co	$(NiCoFeCr)_{92}Al_8$	tracer	229	
Ni	$(NiCoFeCr)_{92}Al_8$	tracer	227	
Cr	NiCoFeCr	tracer	323	[57]
Fe	NiCoFeCr	tracer	303	
Co	NiCoFeCr	tracer	240	
Ni	NiCoFeCr	tracer	253	
Cr	Ni-22Cr	tracer	279	[58]
Ti	Ni	interdiffusion	275	[59]
Cr	Ni	interdiffusion	289	
Co	Ni	interdiffusion	282	
Al	Ni	interdiffusion	268	[60]

Yang *et al.* suggested that their high apparent activation energy for coarsening results from a sluggish-diffusion behavior in the FCC matrix [14]. However, we rather believe that this high value results from the estimation of *Q* for coarsening using an Arrhenius-type fit. Indeed, the temperature dependence of the coarsening rate *K* can be written as:

$$K = \frac{K_0}{T} exp\left(\frac{-Q}{\mathrm{R}T}\right) \tag{6}$$

where K_0 is a term usually considered to be temperature-independent, *T* is the temperature, *Q* is the apparent activation energy for coarsening, and R is the gas constant. The fit of equation 6 to coarsening kinetics data only yields the "true" activation energy when K_0 remains temperature-independent in the investigated temperature range. As the latter is usually not fulfilled in practice, the apparent activation energies must be corrected. Even in the most straightforward cases, considering an ideal solid solution with low volume fractions of precipitates and the existence of a single rate-limiting species *p*, K_0 is obtained by combining equations (3) and (6) as:

$$K_0 = \frac{64\, V_m^{\gamma'} \sigma D_{0,p} C_p^{\gamma} (1 - C_p^{\gamma})}{9\, R (C_p^{\gamma'} - C_p^{\gamma})^2} \tag{7}$$

If the temperature dependence of K_0 is weak, then the activation energy for coarsening *Q* will be close to the activation energy for diffusion of species *p* (Q_p). It is clear from equation (7) that, even in the simple case presented here, K_0 can have a strong temperature dependence.

The assessment of the existence of a rate-limiting species can be helpful in understanding the impact of nominal composition changes on coarsening rates. In the coarsening process, the rate-limiting element *p* is the one that minimizes the product of the diffusion coefficient D_p with a composition-dependent term $X_p = \frac{C_p^{\alpha}(1-C_p^{\alpha})}{(C_p^{\beta}-C_p^{\alpha})^2}$ (equation 3). The values of these terms are given in Table 8 for the TA5 and TA6 alloys at 950°C. To the author's knowledge, no experimental data for diffusion are available for FCC solid solutions in the senary Al–Ti–Cr–Fe–Co–Ni system for temperatures close to 950°C. Chen *et al.* have determined diffusion coefficients at 1200°C in alloys with compositions close to the FCC matrix of TA5 using the inverse

numerical method [61]. However, the temperature dependence was not studied. Hence we used the diffusion coefficients determined by Dąbrowa *et al.* in Al–Cr–Fe–Co–Ni alloys [56]. These values should be taken with care as they do not incorporate the diffusivities of Al and Ti. Nonetheless, they allow a comparison of the impact of Cr, Fe, Co, and Ni on the coarsening rate in both alloys. Of these four elements, Ni has the lowest $D_p \cdot X_p$ product, which is almost one order of magnitude lower than that of the second lowest, obtained for Cr (Table 8).

Table 8: Matrix and precipitate concentrations determined with APT measurements for the TA5 alloy after the 950°C/1.5h heat treatment and diffusion coefficient extrapolated from Ref. [56].

		C_p^{α} (at. %)	C_p^{β} (at. %)	X_p	D_p (m^2/s)	$D_p \cdot X_p$
TA5 (950°C)	Al	4.1	7.7	30.3	-	-
	Ti	3.4	16.8	1.8	-	-
	Cr	19.1	1.6	5.0	1.6×10^{-16}	7.9×10^{-16}
	Fe	23.8	4.9	5.1	1.4×10^{-16}	7.3×10^{-16}
	Co	23.9	16.2	30.7	1.5×10^{-16}	4.7×10^{-15}
	Ni	25.6	52.6	2.6	3.8×10^{-17}	9.9×10^{-17}
TA6 (950°C)	Al	3.8	9.5	11.3	-	-
	Ti	2.4	15.2	1.4	-	-
	Cr	21.0	2.0	4.4	1.6×10^{-16}	7.0×10^{-16}
	Fe	13.6	2.4	9.4	1.4×10^{-16}	1.3×10^{-15}
	Co	29.9	15.8	10.5	1.5×10^{-16}	1.6×10^{-15}
	Ni	29.2	55.5	3.0	3.8×10^{-17}	1.1×10^{-16}

The impact of Al on the coarsening rate in the TA5 alloy should be limited since $X_{Al} = 30.3$ is very high compared to those of the other elements (Table 8). Concerning Ti, Chen *et al.* [61] showed that Ti and Ni have similar diffusion coefficients at 1200°C. Overall, it seems that both Ni and Ti could be rate-limiting species in the coarsening process of the $L1_2$ phase, originating from both a low diffusion coefficient in the FCC matrix and a large difference in concentration between the FCC matrix and precipitates. The same analysis can be carried out for the other alloys using the calculated chemical compositions given by the TCHEA3 database. This analysis leads to the same conclusion for TA4 and TA7, with X_{Ti} being even smaller at lower temperatures.

To correct the apparent activation energies for coarsening, all parameters leading to a variation of K_0 with temperature must be considered individually. In order to do so, the different contributions to $K_0^{950°C}/K_0^{850°C}$ were estimated (see equation 7) and are listed in Table 9. For instance, the contribution of the $L1_2$ volume fraction to this ratio is estimated from equations 4 and 5 and is expressed as $R_{vf} = \frac{K_0^{950°C}(v_f)}{K_0^{850°C}(v_f)}$ with $0.91 <$

$R_{vf} < 0.95$. The impact of volume fraction could very well be neglected since it has been shown that in the presence of coherency stress, the coarsening rate remains constant for intermediate volume fractions (20-50%) [44,62], which is our case. However, since it is not clear whether the lattice mismatch has a significant influence on coarsening, the analysis will be carried out with the case that favors a decrease of the activation energy. The temperature-dependence of the Hessian of the matrix can be readily neglected: the reader is referred to the supplementary material for more details. As the investigated temperature interval is narrow, the contribution of thermal expansion is very small and $V_m^{\gamma'}$(950°C)/ $V_m^{\gamma'}$(850°C) ≈ 1. As a first approximation, the interfacial energy evolution with temperature was taken as equal to that reported for the binary Ni–Al system [40], leading to σ(950°C)/σ(850°C) ≈ 0.9. The ratio $X_i^{950°C}/X_i^{850°C}$ of the i^{th} element was computed using Thermo-Calc and the corresponding values are listed in Table 9. Here, the ratio of the composition dependent parameters for the rate-limiting diffusing element Ti is significant ($1.79 < X_{Ti}^{950°C}/X_{Ti}^{850°C} < 2.79$), thus revealing that the temperature dependence of Ti partitioning between the FCC and $L1_2$ phases strongly affects the temperature dependence of K_0 in equation 7, which in turn results in overestimated apparent activation energies by ~22% for coarsening (Fig. 12).

Table 9: Ratios of the parameters affecting the temperature dependence of K_0. In other words, the $K_0^{950°C}/K_0^{850°C}$ ratio is proportional to the following ratios.

	TA4 (calculated)	**TA5 (calculated)**	**TA7 (calculated)**	**TA6 (calculated)**	**TA6 (APT)**
R_{vf}	0.914	0.931	0.925	0.945	0.952
$V_m^{\gamma'}$(950°C)/ $V_m^{\gamma'}$(850°C)			≃1		
σ(950°C)/σ(850°C)			< 1 (≃0.9)		
Hessian ratio			1 (ideal solid solution)		
$X_{Al}^{950°C}/X_{Al}^{850°C}$	2.21	2.53	2.39	2.37	2.26
$X_{Ti}^{950°C}/X_{Ti}^{850°C}$	2.79	2.55	2.02	2.32	1.79
$X_{Cr}^{950°C}/X_{Cr}^{850°C}$	1.21	1.23	1.27	1.20	1.03
$X_{Fe}^{950°C}/X_{Fe}^{850°C}$	1.24	1.30	1.43	1.27	1.24
$X_{Co}^{950°C}/X_{Co}^{850°C}$	1.24	1.15	1.16	1.20	1.58
$X_{Ni}^{950°C}/X_{Ni}^{850°C}$	1.64	1.81	1.66	1.59	1.42

In other words, considering that Ti is the rate-limiting species in TA6, the correction of its apparent activation energy for $L1_2$ coarsening (352 ± 29 kJ/mol) yields an

approximate value of the activation energy for diffusion of 306 ± 23 kJ/mol and 282 ± 19 kJ/mol using the APT data and the Ti concentrations in the FCC and $L1_2$ phases computed using Thermo-Calc, respectively. These latter two values do not significantly differ from each other's and the average is well within the limits expected for bulk diffusion (Table 7).

To conclude, the high apparent activation energy for coarsening in TA6 and TA7 results from a high partitioning of Ti to the $L1_2$ precipitates. This phenomenon is promoted by increases in Fe and Cr concentrations, which tend to lower the Ti solubility in the FCC matrix [7] and increase its temperature dependence.

4.6 Physical meaning of the apparent activation energy for coarsening

The analyses presented in section 4.5 show that the comparison of activation energy for coarsening with that for diffusion is not straightforward. For instance, the temperature dependence of several parameters must be accounted for to correct the apparent activation energy for coarsening (Q) and retrieve the activation energy for diffusion. Therefore, the sluggish-diffusion argument that was often claimed in the literature to rationalize the abnormally high Q-values in CCAs are irrelevant and should not be used as a blanket statement. It is underlined that the sluggish-diffusion was also questioned in single-phased HEA [63,64]. Furthermore, the Q-values should not be used to determine the rate-limiting species if a thorough analysis of the parameters relevant to coarsening is not made. In our senary alloys from the Al–Ti–Cr–Fe–Co–Ni system, we identified that the temperature dependence of the FCC and $L1_2$ compositions is the main reason for the abnormally high Q-values. However, the limiting point of this correction is the use of reliable thermodynamic databases to compute the volume fraction of phases and their compositions.

5. Conclusions

The coarsening kinetics of $L1_2$ precipitates were investigated in four model alloys to highlight the role of chemical composition: $Al_{7.5}Ti_5Cr_{13.1}Fe_{17.5}Co_{4.4}Ni_{52.5}$ (TA4), $Al_5Ti_{7.5}Cr_{13.1}Fe_{17.5}Co_{21.9}Ni_{35}$ (TA5), $Al_{5.5}Ti_7Cr_{13.1}Fe_{8.8}Co_{25.2}Ni_{40.4}$ (TA6), and $Al_{4.5}Ti_8Cr_{13.1}Fe_{8.8}Co_{37.6}Ni_{28}$ (TA7). Our findings can be summarized as follows:

1. Thermodynamic calculations with the TCNI9 and TCHEA3 thermodynamic databases are in reasonable agreement with APT measurements of the FCC and $L1_2$ compositions, indicating that the former is appropriate for thermo-kinetic modelling.
2. The mean size of $L1_2$ precipitates increases with time following a power law with a time exponent of 3 in the investigated temperature range (850-950°C), indicating that bulk diffusion in the FCC matrix is the rate-controlling phenomenon that governs the coarsening kinetics of the $L1_2$ precipitates in all alloys.
3. Thermo-kinetic modeling using the TC-Prisma module, the TCNI9 thermodynamic database, and MOBNI4 mobility database reproduce the experimental results reasonably well with an interfacial energy taken as 10 mJ/m^2. This agreement suggests that the coarsening kinetics in CCAs is not sluggish as often claimed in the literature.
4. The TA6 and TA7 alloys with 8.8 at.% Fe exhibit lower coarsening rates at 950°C than the TA4 and TA5 alloys with a higher Fe concentration of 17.5 at.%. This effect may result from several contributions: a decrease of the lattice misfit combined with an increase of the interfacial energy between the FCC and $L1_2$ phases. Another possibility is that the interdiffusion coefficient of the CCA increases with Fe additions, but further work is still required to investigate this hypothesis.
5. The TA6 and TA7 alloys have similar coarsening rates between 850 and 950°C, suggesting that Co–Ni and Ti–Al substitutions do not influence the coarsening behavior in the considered concentration range, namely intermediate Ni/Co ratio, 13.1 at.% Cr and 8.8 at.% Fe.
6. The coarsening rate of TA4 is higher than that of TA5 at 950°C suggesting that the substitution of Ni by Co and Al by Ti lowers the coarsening rate of $L1_2$ precipitates in the corresponding concentration range, namely high Ni/Co ratio, 13.1 at.% Cr and 17.5 at.% Fe.
7. If we assume that all four alloys have the same rate-limiting species, as suggested by the present analysis, the differences in coarsening rates could be the result of a higher partitioning coefficient of Ti and/or Ni in the presence of Cr and/or Fe in CCAs.

8. The coarsening rates of the best-performing alloys (*i.e.*, TA6 and TA7) are similar to those of Ni-based superalloys.
9. The apparent activation energies for coarsening were determined to be abnormally high in TA6 and TA7: Q_{TA6} = 352 ± 29 kJ/mol and Q_{TA7} = 360 ± 9 kJ/mol. When the temperature dependences of the FCC and $L1_2$ compositions are accounted for, the corrected activation energies for coarsening are comprised between 280 and 300 kJ/mol, which are in much better agreement with the activation energies for diffusion of Ni and Ti in the CCAs, which diffusion is suspected to be rate controlling.

Our experimental results suggest that thermo-kinetic tools such as Prisma are very effective and could be used to design alloys. The use of this tool in addition to analytical models offers a complementary approach, allowing to obtain a good compromise between thermodynamic stability, low coarsening rates and costs by tailoring the chemical composition. However, further work is required to evaluate the influence of chemical composition on the interfacial energy between matrix and precipitates and interdiffusion coefficients in the matrix, which are key to the coarsening process.

Acknowledgments

TR, JPC, LP, IG and GD would like to acknowledge the French National Research Agency (ANR) for the support through the ANR 16-CE08-0027 “TURBO-AHEAD” program. GL acknowledges funding from the German Research Foundation (Deutsche Forschungsgemeinschaft DFG) through the Priority Program SPP 2006 “Compositionally Complex Alloys - High Entropy Alloys” project LA 3607/3-2. The authors also acknowledge the financial support from the CNRS-CEA “METSA” French network (FR CNRS 3507) for the APT experiments conducted in the GPM laboratory.

References

[1] Q. Wang, Z. Li, S. Pang, X. Li, C. Dong, P. Liaw, Coherent Precipitation and Strengthening in Compositionally Complex Alloys: A Review, Entropy. 20 (2018) 878. https://doi.org/10.3390/e20110878.

[2] T. Yang, Y. Zhao, W. Liu, J. Kai, C. Liu, L12-strengthened high-entropy alloys for advanced structural applications, J. Mater. Res. 33 (2018) 2983–2997. https://doi.org/10.1557/jmr.2018.186.

[3] J.Y. He, H. Wang, H.L. Huang, X.D. Xu, M.W. Chen, Y. Wu, X.J. Liu, T.G. Nieh, K. An, Z.P. Lu, A precipitation-hardened high-entropy alloy with outstanding tensile properties, Acta Mater. 102 (2016) 187–196. https://doi.org/10.1016/j.actamat.2015.08.076.

[4] A. Manzoni, S. Haas, H. Daoud, U. Glatzel, C. Förster, N. Wanderka, Tensile Behavior and Evolution of the Phases in the Al10Co25Cr8Fe15Ni36Ti6 Compositionally Complex/High Entropy Alloy, Entropy. 20 (2018) 646. https://doi.org/10.3390/e20090646.

[5] T.-K. Tsao, A.-C. Yeh, C.-M. Kuo, K. Kakehi, H. Murakami, J.-W. Yeh, S.-R. Jian, The High Temperature Tensile and Creep Behaviors of High Entropy Superalloy, Sci. Rep. 7 (2017). https://doi.org/10.1038/s41598-017-13026-7.

[6] J. Hunfeld, H. Sommer, J. Kiese, H. Wang, A.R. khorasgani, T. Li, C. Somsen, A. Kostka, G. Laplanche, Design of a new wrought CrCoNi-based medium-entropy superalloy C-264 for high-temperature applications, Mater. Des. 211 (2021) 110174. https://doi.org/https://doi.org/10.1016/j.matdes.2021.110174.

[7] T. Rieger, J.-M. Joubert, M. Laurent-Brocq, L. Perrière, I. Guillot, J.-P. Couzinié, Study of the FCC+L12 two-phase region in complex concentrated alloys based on the Al–Co–Cr–Fe–Ni–Ti system, Materialia. 14 (2020) 100905. https://doi.org/10.1016/j.mtla.2020.100905.

[8] Y.Y. Zhao, H.W. Chen, Z.P. Lu, T.G. Nieh, Thermal stability and coarsening of coherent particles in a precipitation-hardened (NiCoFeCr) 94 Ti 2 Al 4 high-entropy alloy, Acta Mater. 147 (2018) 184–194. https://doi.org/10.1016/j.actamat.2018.01.049.

[9] J.-W. Yeh, Recent progress in high entropy alloys, Ann Chim Sci Mat. 31 (2006) 633–648.

[10] S. Adil, M.V. Suraj, L.K. Pillari, S. Sridar, M. Nagini, K.G. Pradeep, B.S. Murty, On the effect of Fe in L12 strengthened Al–Co–Cr–Fe–Ni–Ti complex concentrated alloy, Materialia. 14 (2020) 100909. https://doi.org/10.1016/j.mtla.2020.100909.

[11] F. He, K. Zhang, G. Yeli, Y. Tong, D. Wei, J. Li, Z. Wang, J. Wang, J. Kai, Anomalous effect of lattice misfit on the coarsening behavior of multicomponent L12 phase, Scr. Mater. 183 (2020) 111–116. https://doi.org/10.1016/j.scriptamat.2020.03.030.

[12] H. Peng, L. Hu, L. Li, J. Gao, Q. Zhang, On the correlation between L12 nanoparticles and mechanical properties of (NiCo)52+2x(AlTi)4+2xFe29-4xCr15 (x=0-4) high-entropy alloys, J. Alloys Compd. 817 (2020) 152750. https://doi.org/10.1016/j.jallcom.2019.152750.

[13] P. Pandey, S. Kashyap, D. Palanisamy, A. Sharma, K. Chattopadhyay, On the high temperature coarsening kinetics of gamma prime precipitates in a high strength Co37.6Ni35.4Al9.9Mo4.9Cr5.9Ta2.8Ti3.5 fcc-based high entropy alloy, Acta Mater. 177 (2019) 82–95. https://doi.org/10.1016/j.actamat.2019.07.011.

[14] T. Yang, Y.L. Zhao, L. Fan, J. Wei, J.H. Luan, W.H. Liu, C. Wang, Z.B. Jiao, J.J. Kai, C.T. Liu, Control of nanoscale precipitation and elimination of intermediate-temperature embrittlement in multicomponent high-entropy alloys, Acta Mater. 189 (2020) 47–59. https://doi.org/10.1016/j.actamat.2020.02.059.

[15] H.A. Calderon, P.W. Voorhees, J.L. Murray, G. Kostorz, Ostwald ripening in concentrated alloys, Acta Metall. Mater. 42 (1994) 991–1000.

[16] C.T. Sims, A history of superalloy metallurgy for superalloy metallurgists, Superalloys. 1984 (1984) 399–419.

[17] F. Stein, M. Merali, P. Watermeyer, The Co–Ti system revisited: About the cubic-to-hexagonal Laves phase transformation and other controversial features of the phase diagram, Calphad. 67 (2019) 101681. https://doi.org/https://doi.org/10.1016/j.calphad.2019.101681.
[18] J.M. Blaise, P. Viatour, J.M. Drapier, On the stability and precipitation of the Co3Ti phase in Co-Ti alloys, Cobalt. (1970).
[19] P. Viatour, J.M. Drapier, D. Coutsouradis, Stability of the gamma prime Co3Ti compound in simple and complex Co alloys, Cobalt. (1973).
[20] X. Bai, W. Fang, J. lv, R. Chang, H. Yu, J. Yan, X. Zhang, F. Yin, Effect of Cr content on precipitation behavior of (CoCrNi)94Ti3Al3 medium entropy alloys, Intermetallics. 132 (2021) 107125. https://doi.org/10.1016/j.intermet.2021.107125.
[21] J. Rodriguez-Carvajal, FULLPROF: A Program for Rietveld Refinement and Pattern Matching Analysis, Abstr. Satell. Meet. Powder Diffr. XV Congr. IUCr. Toulouse, France (1990) 127.
[22] Y. Wang, A.G. Khachaturyan, Shape instability during precipitate growth in coherent solids, Acta Metall. Mater. 43 (1995) 1837–1857. https://doi.org/https://doi.org/10.1016/0956-7151(94)00406-8.
[23] A.J. Ardell, Trans-interface-diffusion-controlled coarsening of γ′ particles in Ni–Al alloys: commentaries and analyses of recent data, J. Mater. Sci. 55 (2020) 14588–14610. https://doi.org/10.1007/s10853-020-05036-0.
[24] T. Philippe, P.W. Voorhees, Ostwald ripening in multicomponent alloys, Acta Mater. 61 (2013) 4237–4244. https://doi.org/10.1016/j.actamat.2013.03.049.
[25] I.M. Lifshitz, V.V. Slyozov, The kinetics of precipitation from supersaturated solid solutions, J. Phys. Chem. Solids. 19 (1961) 35–50.
[26] A. Baldan, Review progress in Ostwald ripening theories and their applications to nickel-base superalloys Part I: Ostwald ripening theories, J. Mater. Sci. 37 (2002) 2171–2202.
[27] A.J. Ardell, Trans-interface-diffusion-controlled coarsening of γ′ precipitates in ternary Ni–Al–Cr alloys, Acta Mater. 61 (2013) 7828–7840. https://doi.org/10.1016/j.actamat.2013.09.021.
[28] A.J. Ardell, V. Ozolins, Trans-interface diffusion-controlled coarsening, Nat. Mater. 4 (2005) 309–316. https://doi.org/10.1038/nmat1340.
[29] B.A. Pletcher, K.-G. Wang, M.E. Glicksman, Ostwald ripening in Al–Li alloys: A test of theory, Int. J. Mater. Res. 103 (2012) 1289–1293.
[30] M.E. Glicksman, K.-G. Wang, S.P. Marsh, Diffusional interactions among crystallites, J. Cryst. Growth. 230 (2001) 318–327.
[31] K.G. Wang, M.E. Glicksman, K. Rajan, Modeling and simulation for phase coarsening: A comparison with experiment, Phys. Rev. E. 69 (2004). https://doi.org/10.1103/PhysRevE.69.061507.
[32] Precipitation Module (TC-PRISMA) User Guide, (n.d.). https://www.thermocalc.com/content/uploads/Documentation/Current_Static/precipitation-module-tc-prisma-user-guide.pdf (accessed October 15, 2021).
[33] G. Kostorz, ed., Phase transformations in materials, New ed., Wiley-VCH, Weinheim ; New York ; Chichester, 2001.
[34] S. Meher, M.C. Carroll, T.M. Pollock, L.J. Carroll, Designing nickel base alloys for microstructural stability through low γ-γ′ interfacial energy and lattice misfit, Mater. Des. 140 (2018) 249–256. https://doi.org/10.1016/j.matdes.2017.11.065.
[35] X. Li, N. Saunders, A.P. Miodownik, The coarsening kinetics of γ′ particles in nickel-based alloys, Metall. Mater. Trans. A. 33 (2002) 3367–3373.
[36] C.K.L. Davies, P. Nash, R.N. Stevens, The effect of volume fraction of precipitate on Ostwald ripening, Acta Metall. 28 (1980) 179–189.
[37] C. Liu, Y. Li, L. Zhu, S. Shi, S. Chen, S. Jin, Morphology and kinetics evolution of γ′ phase with increased volume fraction in Ni–Al alloys, Mater. Chem. Phys. 217 (2018) 23–30. https://doi.org/10.1016/j.matchemphys.2018.06.038.

[38] J. Chen, M. Guo, M. Yang, H. Su, L. Liu, J. Zhang, Phase-field simulation of γ' coarsening behavior in cobalt-based superalloy, Comput. Mater. Sci. 191 (2021) 110358. https://doi.org/https://doi.org/10.1016/j.commatsci.2021.110358.
[39] X.L. Liu, S.-L. Shang, Y.-J. Hu, Y. Wang, Y. Du, Z.-K. Liu, Insight into γ-Ni/γ′-Ni3Al interfacial energy affected by alloying elements, Mater. Des. 133 (2017) 39–46.
[40] G. Kaptay, On the interfacial energy of coherent interfaces, Acta Mater. 60 (2012) 6804–6813. https://doi.org/10.1016/j.actamat.2012.09.002.
[41] M.G. Fahrmann, D.A. Metzler, Simulation of γ′ Precipitation Kinetics in a Commercial Ni-Base Superalloy, JOM. 68 (2016) 2786–2792. https://doi.org/10.1007/s11837-016-2097-5.
[42] T. Hara, S. Kobayashi, T. Ueno, K. Oikawa, Estimation of γ/γ′ interfacial energy in Ni-Co base superalloy TMW-4M3, J. Cryst. Growth. 506 (2019) 91–96. https://doi.org/10.1016/j.jcrysgro.2018.10.014.
[43] V.J. Larala, W.C. Johnson, P.W. Voorhees, The kinetics of ostwald ripening in stressed solids: The low volume fraction limit, Scr. Metall. 23 (1989) 1749–1754.
[44] V. Vaithyanathan, L.Q. Chen, Coarsening of ordered intermetallic precipitates with coherency stress, Acta Mater. 50 (2002) 4061–4073. https://doi.org/https://doi.org/10.1016/S1359-6454(02)00204-5.
[45] C. Liu, Y. Li, L. Zhu, S. Shi, Effect of Coherent Lattice Mismatch on the Morphology and Kinetics of Ordered Precipitates, J. Mater. Eng. Perform. 27 (2018) 4968–4977. https://doi.org/10.1007/s11665-018-3572-7.
[46] J.G. Conley, M.E. Fine, J.R. Weertman, Effect of lattice disregistry variation on the late stage phase transformation behavior of precipitates in Ni□ Al□ Mo alloys, Acta Metall. 37 (1989) 1251–1263.
[47] M.E. Thompson, C.S. Su, P.W. Voorhees, The equilibrium shape of a misfitting precipitate, Acta Metall. Mater. 42 (1994) 2107–2122.
[48] S.C.H. Llewelyn, L.R. Owen, H.Y. Playford, N.G. Jones, D. Dye, M.C. Hardy, H.J. Stone, Influence of Ni:Co ratio and temperature on the lattice misfit of γ-γ' Ni-Co-Al-Ti-Cr alloys, J. Alloys Compd. 937 (2023) 168253. https://doi.org/https://doi.org/10.1016/j.jallcom.2022.168253.
[49] A.M. Irisarri, J.. Urcola, M. Fuentes, Kinetics of growth of gamma prime -precipitates in Ni- 6.75Al alloy, Mater Sci Technol. 1 (1985) 516–519.
[50] C.S. Jayanth, P. Nash, Experimental evaluation of particle coarsening theories, Mater. Sci. Technol. 6 (1990) 405–414.
[51] S. Meher, S. Nag, J. Tiley, A. Goel, R. Banerjee, Coarsening kinetics of γ′ precipitates in cobalt-base alloys, Acta Mater. 61 (2013) 4266–4276. https://doi.org/10.1016/j.actamat.2013.03.052.
[52] P.K. Footner, B.P. Richards, Long—term growth of superalloy γ′ particles, J. Mater. Sci. 17 (1982) 2141–2153.
[53] J. Lapin, M. Gebura, T. Pelachová, M. Nazmy, Coarsening kinetics of cuboidal γ'precipitates in single crystal nickel base superalloy CMSX-4, Kov. Mater. 46 (2008) 313–322.
[54] K. Zhang, F. He, Z. Yang, D. Cui, J. Li, Z. Yang, J. Wang, Z. Wang, Effect of Re and Ru on the phase stability and coarsening kinetics of L12 phase in a Ni29Co27Fe27Cr3Al7Ti7 high entropy alloy, J. Alloys Compd. 866 (2021) 158904. https://doi.org/10.1016/j.jallcom.2021.158904.
[55] W. Yang, H. Zong, C. Yang, P. Qu, H. Su, Y. Dong, J. Zhang, L. Liu, The effect of Fe addition on γ′ precipitates during thermal exposure in Ni-Co-based single crystal superalloys, J. Mater. Res. Technol. 20 (2022) 894–904. https://doi.org/https://doi.org/10.1016/j.jmrt.2022.07.135.
[56] J. Dabrowa, W. Kucza, G. Cieślak, T. Kulik, M. Danielewski, J.-W. Yeh, Interdiffusion in the FCC-structured Al-Co-Cr-Fe-Ni high entropy alloys: Experimental studies and numerical simulations, J. Alloys Compd. 674 (2016) 455–462. https://doi.org/10.1016/j.jallcom.2016.03.046.

[57] M. Vaidya, S. Trubel, B.S. Murty, G. Wilde, S.V. Divinski, Ni tracer diffusion in CoCrFeNi and CoCrFeMnNi high entropy alloys, J. Alloys Compd. 688 (2016) 994–1001. https://doi.org/10.1016/j.jallcom.2016.07.239.
[58] T. Gheno, F. Jomard, C. Desgranges, L. Martinelli, Tracer diffusion of Cr in Ni and Ni-22Cr studied by SIMS, Materialia. 3 (2018) 145–152. https://doi.org/10.1016/j.mtla.2018.08.004.
[59] S.B. Jung, T. Yamane, Y. Minamino, K. Hirao, H. Araki, S. Saji, Interdiffusion and its size effect in nickel solid solutions of Ni-Co, Ni-Cr and Ni-Ti systems, J. Mater. Sci. Lett. 11 (1992) 1333–1337.
[60] R.A. Swalin, A. Martin, Solute diffusion in nickel-base substitutional solid solutions, J Met. Vol (1956). https://www.osti.gov/biblio/4356254.
[61] S. Chen, Q. Li, J. Zhong, F. Xing, L. Zhang, On diffusion behaviors in face centered cubic phase of Al-Co-Cr-Fe-Ni-Ti high-entropy superalloys, J. Alloys Compd. 791 (2019) 255–264. https://doi.org/10.1016/j.jallcom.2019.03.286.
[62] D.M. Kim, A.J. Ardell, The volume-fraction dependence of Ni3Ti coarsening kinetics—new evidence of anomalous behavior, Scr. Mater. 43 (2000) 381–384. https://doi.org/https://doi.org/10.1016/S1359-6462(00)00439-5.
[63] J. Kottke, M. Laurent-Brocq, A. Fareed, D. Gaertner, L. Perrière, Ł. Rogal, S.V. Divinski, G. Wilde, Tracer diffusion in the Ni–CoCrFeMn system: Transition from a dilute solid solution to a high entropy alloy, Scr. Mater. 159 (2019) 94–98. https://doi.org/10.1016/j.scriptamat.2018.09.011.
[64] J. Dabrowa, M. Zajusz, W. Kucza, G. Cieslak, K. Berent, T. Czeppe, T. Kulik, M. Danielewski, Demystifying the sluggish diffusion effect in high entropy alloys, J. Alloys Compd. 783 (2019) 193–207. https://doi.org/10.1016/j.jallcom.2018.12.300.